

LETTER • OPEN ACCESS

Rain-fed pulses of methane from East Africa during 2018–2019 contributed to atmospheric growth rate

To cite this article: Mark F Lunt *et al* 2021 *Environ. Res. Lett.* **16** 024021

View the [article online](#) for updates and enhancements.

ENVIRONMENTAL RESEARCH
LETTERS

LETTER

OPEN ACCESS

RECEIVED

29 September 2020

REVISED

10 December 2020

ACCEPTED FOR PUBLICATION

6 January 2021

PUBLISHED

3 February 2021

Original Content from this work may be used under the terms of the [Creative Commons Attribution 4.0 licence](#).

Any further distribution of this work must maintain attribution to the author(s) and the title of the work, journal citation and DOI.



Rain-fed pulses of methane from East Africa during 2018–2019 contributed to atmospheric growth rate

Mark F Lunt¹ , Paul I Palmer^{1,2} , Alba Lorente³ , Tobias Borsdorff³ , Jochen Landgraf³ , Robert J Parker^{4,5} and Hartmut Boesch^{4,5} ¹ School of GeoSciences, University of Edinburgh, Edinburgh, United Kingdom² National Centre for Earth Observation, University of Edinburgh, Edinburgh, United Kingdom³ Earth Science Group, SRON Netherlands Institute for Space Research, Utrecht, The Netherlands⁴ National Centre for Earth Observation, University of Leicester, Leicester, United Kingdom⁵ Earth Observation Science, School of Physics and Astronomy, University of Leicester, Leicester, United KingdomE-mail: mark.lunt@ed.ac.uk**Keywords:** methane, East Africa, wetlands, Indian Ocean DipoleSupplementary material for this article is available [online](#)**Abstract**

East Africa is a key location for wetland emissions of methane (CH₄), driven by variations in rainfall that are in turn influenced by sea-surface temperature gradients over the Indian Ocean. Using satellite observations of CH₄ and an atmospheric chemistry-transport model, we quantified East African CH₄ emissions during 2018 and 2019 when there was 3- σ anomalous rainfall during the long rains (March–May) in 2018 and the short rains (October–December) in 2019. These rainfall anomalies resulted in CH₄ emissions of 6.2 ± 0.3 Tg CH₄ and 8.6 ± 0.3 Tg CH₄, in each three month period, respectively, and represent a 10% and 37% increase compared to the equivalent season in the opposite year, when rainfall was close to the long-term seasonal mean. We find the additional short rains emissions were equivalent to over a quarter of the growth in global emissions in 2019, highlighting the disproportionate role of East Africa in the global CH₄ budget.

1. Introduction

The atmospheric concentration of methane (CH₄), an important greenhouse gas, has continued to rise through the 20th century with only a brief respite early this century between 2000 and 2007. In recent years, there has been particularly strong global mean annual growth, partly driven by pan-tropical variations due to the 2014/2015 El Niño (Zhang *et al* 2018). Generally, these observed variations have defied any definitive explanation with several competing plausible hypotheses that attribute most changes to a particular emission source (e.g. fires, wetlands, oil and gas, agriculture), or to changes in the oxidation loss by the hydroxyl radical (Rigby *et al* 2017, Worden *et al* 2017, McNorton *et al* 2018, Turner *et al* 2019, Saunio *et al* 2020). In practice, on a global scale some combination of changing emissions and loss terms are likely responsible. Previous studies have used a range of data to examine changes on large spatial scales, and the newer satellite data, in particular, provide constraints on regional emission estimates (Hu *et al* 2018, Lunt *et al* 2019).

Recent work has highlighted the important role of East Africa in the global CH₄ budget (Lunt *et al* 2019). The primary sources of CH₄ in Africa are largely microbial with wetlands, agriculture and waste sources contributing an estimated 65% of total emissions (Saunio *et al* 2016). Wetlands emit CH₄ due to the decomposition of organic matter under anaerobic conditions. At large scales, wetland emissions can be broadly explained by three main controls: temperature, carbon availability and water table depth (Moore *et al* 1998, Christensen *et al* 2003, Gedney 2004, Bloom *et al* 2010). In the tropics, where temperature is less of a limiting factor, the dominant control is water table depth (Bloom *et al* 2010, Bloom *et al* 2012, Lunt *et al* 2019). Precipitation anomalies that help drive changes in the water table are linked to wetland CH₄ emission anomalies (Pandey *et al* 2017), taking into account upstream catchment areas and other basin hydrological factors. Emissions from agriculture, particularly ruminants, may also be affected by water controls. Previous work has shown a strong relationship between dry matter intake and CH₄ production in forage-fed cattle (Charmley *et al* 2016).

In East Africa, seasonal changes in the availability of feed affects the seasonal variation of cattle live weight and associated CH₄ production (Ndung'u *et al* 2019).

The wet seasons in East Africa follow the movement of the inter-tropical convergence zone. Northern regions such as Sudan and northern Ethiopia have one wet season which normally peaks in July–September. In contrast regions in the south such as southern Tanzania have a wet season peak in January–March. The region in between, including Kenya and southern Ethiopia, experiences two main wet seasons in March–May (MAM) and October–December (OND) (Herrmann and Mohr 2011). These two wet seasons are termed the long rains and short rains, respectively, and are the focus of this paper.

Large changes in the atmospheric growth of CH₄ in 2019 (Dlugokencky 2020) coincided with an extreme positive index of the Indian Ocean Dipole (IOD) (Lu and Ren 2020). A positive IOD index corresponds to warmer ocean temperatures in the western Indian ocean and cooler temperatures in the eastern Indian Ocean (Saji *et al* 1999). In 2019 this resulted in monthly East African precipitation levels during OND that were one of the wettest short rains seasons on record (Wainwright *et al* 2020). This followed anomalously high precipitation levels during the MAM 2018 long rains (Kilavi *et al* 2018). Here, we use satellite observations of CH₄ from two independent instruments to investigate the impact of these precipitation anomalies on CH₄ emissions from East Africa.

2. Data and methodology

2.1. Satellite data

Two CH₄ satellite datasets are used in this study to examine changes over East Africa: TROPOMI and GOSAT. TROPOMI measures, amongst others, short wave infrared (SWIR) radiances around 2.3 μm. To calculate column-averaged CH₄ concentrations (XCH₄) a physics-based retrieval is used, making use of the Oxygen A-band around 760 nm to infer information about the scattering properties of the atmosphere. The satellite is in a Sun-synchronous orbit with an overpass time of 13:30 local solar time. TROPOMI has a swath width of 2600 km and a ground pixel of 7 × 7 km². We use the scientific CH₄ data product (Lorente *et al* 2020), which implements the RemoTec retrieval algorithm (Butz *et al* 2011, Hu *et al* 2016), and use bias-corrected XCH₄ in our analysis, with the bias correction supplied in the data (Lorente *et al* 2020). Only data with a quality flag of greater than 0.5 are used, which filters data for clouds, high solar and viewing zenith angles and high aerosol loading. In addition we filter the data based on where the SWIR surface albedo is in the range 0.05–0.30, the aerosol optical thickness (AOT) is less than 0.1, and the standard deviation of surface topography in each retrieved pixel is less than 60 m. Initial tests revealed

some anomalously low value data values surviving through these filters, so we further filter the data based on where the difference between observed values and the simulated model background levels within the domain are greater than −5 ppb. We use data over the spatial domain of our model simulations which covers −36 to +20° N and −20 to 55° E.

GOSAT is in a Sun-synchronous orbit with a local equator crossing time of 13:00, resulting in global coverage every three days (Kuze *et al* 2009). We use data from the Thermal And Near infrared Sensor for carbon Observations—Fourier Transform Spectrometer (TANSO-FTS) that measures short wave infrared (SWIR) radiances between 0.76 and 2.0 μm at a resolution of 0.3 cm^{−1} (Parker *et al* 2011). We use the University of Leicester's (UoL) v9 GOSAT-OCPR proxy XCH₄ product (Parker *et al* 2020a). This retrieval algorithm uses a different approach to TROPOMI to calculate XCH₄, relying on the co-retrieved CO₂ column. Taking the ratio between CH₄ and CO₂ can account for factors that impact the retrievals, such as aerosol and cloud scattering. An advantage of this proxy approach is that it is more robust than the full physics approach in the presence of clouds and aerosols. However, the proxy approach does rely on having good knowledge of the true CO₂ distribution in the atmosphere, and errors in this could impact on the derived XCH₄ values. As such, both the full physics and proxy approaches have their strengths and weaknesses. Due to the greater spatial coverage of TROPOMI the number of successful retrievals is far greater than from GOSAT (figure S1). Both datasets have been validated against ground-based data from the Total Carbon Column Observing Network (TCCON) (Wunch *et al* 2011). For both datasets we average the data into 0.25° × 0.3125° pixels to create a set of super-observations at a resolution consistent with the GEOS-Chem atmospheric transport model.

Rainfall data in this study are taken from the TAMSAT (v3.1) monthly precipitation dataset (Maidment *et al* 2014, Tarnavsky *et al* 2014, Maidment *et al* 2017). The data are based on high-resolution thermal-infrared observations and available from 1983 to the present. Rainfall anomalies reported in this work are relative to the 1983–2012 monthly mean. To examine changes in terrestrial water storage we use data from the GRACE Follow-On (GRACE-FO) mission (Landerer *et al* 2020). The GRACE-FO dataset provides monthly liquid water equivalent (LWE) estimates at a resolution of 3° × 3°. Anomalies are relative to the consistent longer-term GRACE dataset 2002–2017 monthly means.

2.2. GEOS-Chem chemistry transport model

We use the GEOS-Chem chemistry transport model to simulate the emissions and transport of atmospheric methane (Bey *et al* 2001, Turner *et al* 2015). The model was run in a nested configuration with a spatial resolution of 0.25° × 0.3125° driven by

offline meteorology fields from the GEOS-FP analysis product. The model has 47 vertical levels. The temporal resolution of the meteorology fields was hourly and the transport and chemistry time steps were five and ten minutes respectively. The nested domain covered -36 to 20° N and -20 to 55° E, encompassing sub-Saharan Africa.

A priori CH₄ emissions within the nested domain mostly followed those used in previous published work (Maasackers *et al* 2019), with anthropogenic emissions for 2012 from EDGAR v4.3.2, and wetland emissions for 2015 from the WetCHARTs dataset (Bloom *et al* 2017). Wetland emissions varied monthly and the anthropogenic emissions included a monthly varying seasonal cycle for manure emissions and rice. Daily biomass burning emissions for 2018–2019 were taken from the GFAS database (Kaiser *et al* 2012). Offline loss fields were included accounting for oxidation by the hydroxyl and chlorine radicals, as well as soil absorption (Wecht *et al* 2014).

Boundary conditions to the nested domain were created from a global run of the GEOS-Chem model run at $2^\circ \times 2.5^\circ$, with 3 h output fields. These fields were sampled at the time and location of GOSAT data, and column average XCH₄ values compared to the data after applying the GOSAT averaging kernels. To create more realistic boundary condition fields that were consistent with the observed zonal distribution of CH₄, these model fields were then scaled to match the GOSAT zonal monthly mean concentrations within a domain of -50° E to 100° E, encompassing data over the Atlantic and Indian oceans. GOSAT data from within the nested African domain were not included in this zonal mean comparison to avoid using these data twice.

The zonal mean of each 2° latitudinal grid cell in the model is thus consistent with the equivalent zonal mean of GOSAT data. However, the vertical and longitudinal distributions of the field are reliant on the *a priori* emissions fields and GEOS-Chem model transport. The boundary conditions thus represent a reasonable approximation to the true atmospheric field at the boundaries of the nested domain and are consistent with the satellite data which is important to negate any global or latitudinal biases in the data or model. The same boundary conditions were used for both TROPOMI and GOSAT inversions, although due to an offset between the two satellites the boundary conditions from TROPOMI were adjusted according to the global mean ratio between the two satellite datasets each month. The impact of using alternative boundary condition fields on our results is explored in the supplementary material (available online at stacks.iop.org/ERL/16/024021/mmedia).

2.3. Emissions estimation

To estimate CH₄ emissions we use an Ensemble Kalman Filter (EnKF) system. Here, we use a variant called the Local Ensemble Transform Kalman Filter

(LETKF) (Hunt *et al* 2007) which has been applied in various previous atmospheric inversions to infer emissions (Miyazaki *et al* 2012, Liu *et al* 2016). We briefly describe the LETKF here, and refer the reader to Hunt *et al* (2007) for an in-depth description.

The LETKF transforms a background ensemble of emissions \mathbf{x}^b with k ensemble members into an analysis ensemble \mathbf{x}^a . The emissions ensemble is defined by its mean $\bar{\mathbf{x}}^b$ and ensemble perturbations \mathbf{X}^b given by:

$$\mathbf{X}^b = \mathbf{x}^b - \bar{\mathbf{x}}^b. \quad (1)$$

The GEOS-Chem model is used to create the operator, H that propagates the emissions ensemble into the observation space following:

$$\mathbf{y}^b = H \cdot \mathbf{x}^b. \quad (2)$$

Ensemble perturbations in the measurement space, \mathbf{Y}^b , are similarly defined to the emissions space as:

$$\mathbf{Y}^b = \mathbf{y}^b - \bar{\mathbf{y}}^b. \quad (3)$$

The background ensemble, \mathbf{x}^b , is updated to an analysis ensemble \mathbf{x}^a , based on the data, \mathbf{y}^o , and calculated by:

$$\bar{\mathbf{x}}^a = \bar{\mathbf{x}}^b + \mathbf{X}^b \cdot \tilde{\mathbf{P}}^a \cdot (\mathbf{Y}^b)^T \mathbf{R}^{-1} \cdot (\mathbf{y}^o - \bar{\mathbf{y}}^b), \quad (4)$$

where \mathbf{R} is the observation error covariance matrix, and \mathbf{R}^{-1} its matrix inverse. $\tilde{\mathbf{P}}^a$ is the local analysis error covariance matrix estimated in the ensemble space, and given by:

$$\tilde{\mathbf{P}}^a = [(\mathbf{Y}^b)^T \mathbf{R}^{-1} \mathbf{Y}^b + (k-1)\mathbf{I}]^{-1}. \quad (5)$$

The updated ensemble perturbations can be calculated according to:

$$\mathbf{X}^a = \mathbf{X}^b [(k-1)\tilde{\mathbf{P}}^a]^{1/2}. \quad (6)$$

Finally, the *a posteriori* analysis error covariance matrix is equal to:

$$\mathbf{P}^a = \mathbf{X}^a (\mathbf{X}^a)^T \frac{1}{k-1}. \quad (7)$$

The diagonals of \mathbf{P}^a represent the uncertainties of the *a posteriori* emissions. In our implementation of the LETKF, the state vector, \mathbf{x} , describes a vector of scale factors applied to the *a priori* emissions field, with each term in \mathbf{x} representing a box of horizontal dimension $0.5^\circ \times 0.625^\circ$. Our *a posteriori* emissions are calculated by multiplying the *a posteriori* scale factors by the *a priori* emission magnitudes. Unless otherwise stated, all results represent total CH₄ emissions from the sum of all sources.

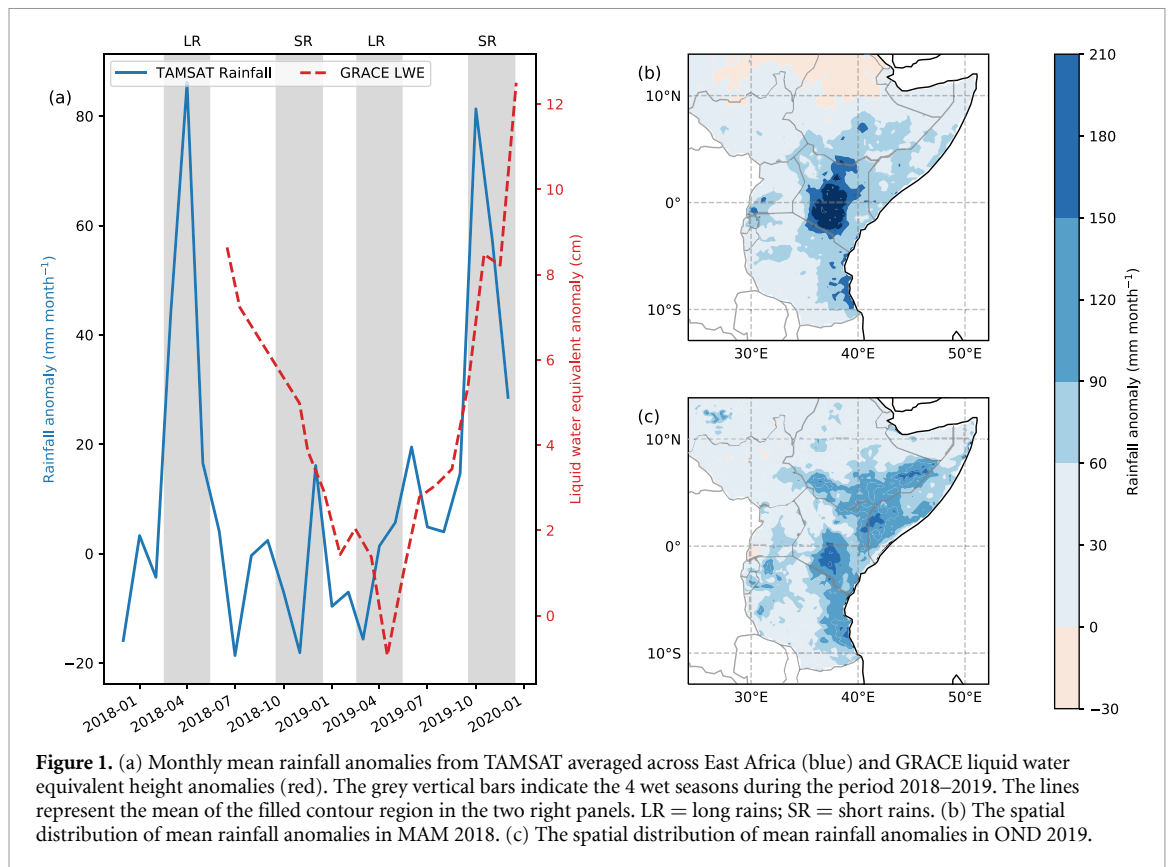


Figure 1. (a) Monthly mean rainfall anomalies from TAMSAT averaged across East Africa (blue) and GRACE liquid water equivalent height anomalies (red). The grey vertical bars indicate the 4 wet seasons during the period 2018–2019. The lines represent the mean of the filled contour region in the two right panels. LR = long rains; SR = short rains. (b) The spatial distribution of mean rainfall anomalies in MAM 2018. (c) The spatial distribution of mean rainfall anomalies in OND 2019.

We used an ensemble of 140 members, a temporal assimilation window of 15 days, and lag window of 1 month. *A priori* emission uncertainties of each grid cell were set to be 200% of the value of each grid cell. In the LETKF, we applied a spatial localization of 800 km that limits the set of observations that are used in the analysis of each state vector element to be within this distance. The diagonal terms of the measurement covariance matrix, \mathbf{R} , were formed from a combination of the measurement retrieval *a posteriori* uncertainties provided in the TROPOMI and GOSAT data files and a modelling uncertainty of 4 ppb, based on the global mean bias of the satellite columns versus TCCON data (Lorente *et al* 2020, Parker *et al* 2020a). We defined off-diagonal terms of \mathbf{R} , to follow an exponential spatial covariance that decayed with a length scale of 50 km. We tested the impact of the inversion parameter definitions on our results through a series of sensitivity tests (see supplementary material).

3. Results

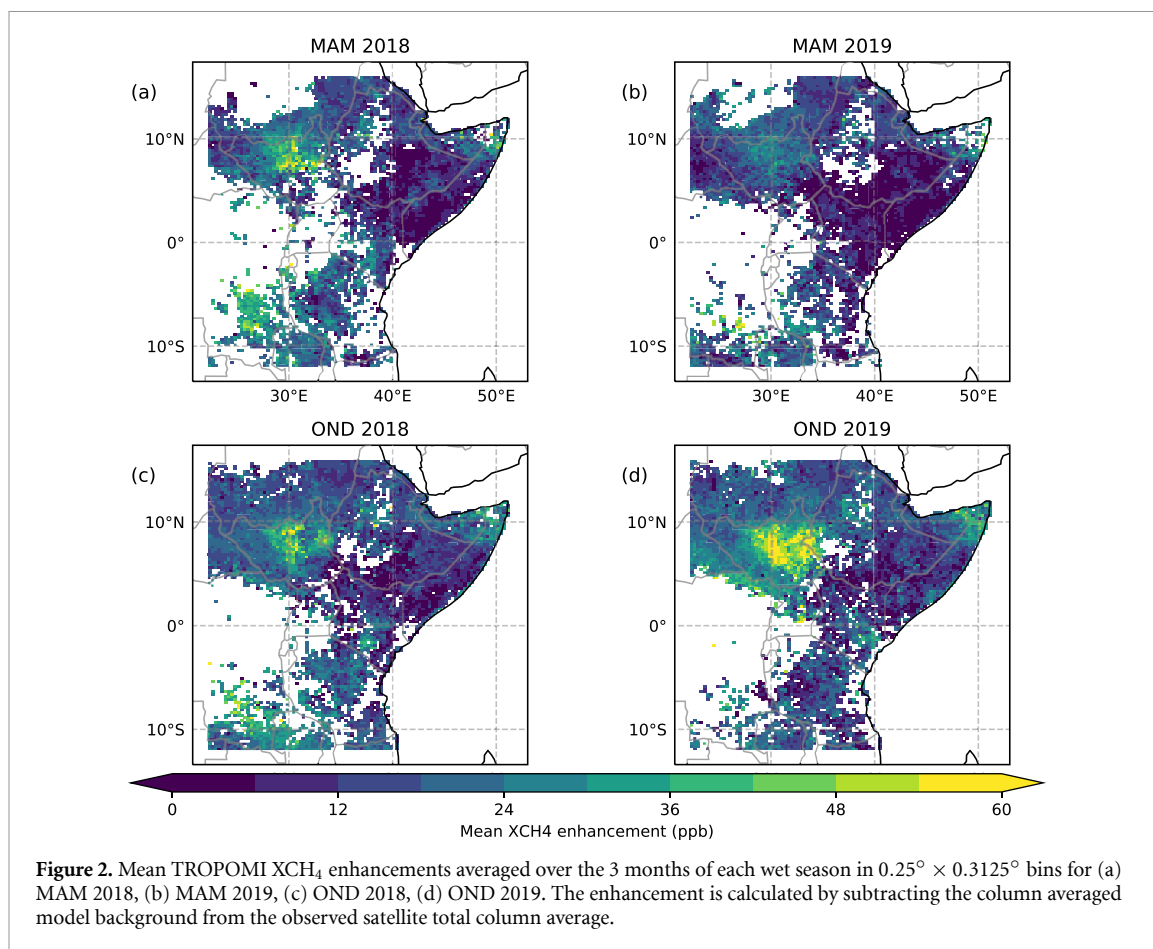
3.1. Rainfall anomalies over East Africa

Between December 2017 and December 2019 there were two notable positive rainfall anomalies: the long rains season of MAM 2018, and the short rains season of OND 2019 (figure 1(a)). The long rains anomaly in 2018, peaked in April with 86 mm month^{-1} , relative to the 1983–2012 mean. The short rains anomaly in 2019, peaked in October with 81 mm month^{-1} .

The standard deviation of monthly anomalies over the 38-year self-consistent data record was 17 mm month^{-1} so that both rainfall anomalies exceed the 3σ level, approximately equivalent to a once in a 30-year event. The 30-year mean rainfall peak in April was 88 mm month^{-1} , and 67 mm month^{-1} in October, showing that these anomalies represent at least double the normal amount of rainfall across the region.

These two large seasonal anomalies had contrasting spatial distributions. The MAM 2018 anomalies were principally over Kenya, Tanzania and Ethiopia (figure 1(b)), while the anomalies during OND 2019 were also over Somalia, Uganda and South Sudan (figure 1(c)). In contrast the wet seasons in OND 2018 and MAM 2019 were close to climatological mean values, with mean anomalies of -3 mm month^{-1} in both OND 2018 and MAM 2019.

A similar, albeit smoother, pattern of anomalies is seen in liquid water equivalent (LWE) height anomalies in East Africa from the GRACE-FO mission (Landerer *et al* 2020) (figure 1(a)), between 2018–07 and 2019–12. The data show a minimum reached in 2019–04, before an increase in the latter part of 2019. Previous studies used LWE anomalies to isolate wetland emissions of CH_4 using satellite column measurements of CH_4 (Bloom *et al* 2010, Bloom *et al* 2012), implying likely changes in wetland emission anomalies as a result of the LWE changes during this period.



3.2. XCH₄ enhancements from TROPOMI

Corresponding seasonal mean XCH₄ enhancements over East Africa (figure 2) are calculated by subtracting a model background component from the XCH₄ column. The model background component is generated by including only that part of the modelled CH₄ field that originated from outside the regional domain in the GEOS-Chem simulation. We assume that the dominant factor affecting XCH₄ enhancements is surface emissions, acknowledging that any errors in generating the modelled background component will affect this quantity. Gaps in the XCH₄ data are due to cloud coverage, surface albedo or aerosol interference preventing successful retrievals; some seasonal mean values may be indicative of only a few successful retrievals in that season (figure S2).

We find the largest XCH₄ enhancements over the Sudd wetlands in South Sudan and the Sobat basin to its east, which are present in OND 2018 and 2019. October represents the end of the wet season in South Sudan, but it is usually the time of peak flooding of the Sudd, due to inflow from the region to the south known as the torrents (Sutcliffe and Parks 1999, Lunt *et al* 2019). In MAM 2018 large XCH₄ enhancements (mean 17 ppb; max 93 ppb) are observed in South Sudan and regions south and east of Lake Victoria. In contrast, in MAM 2019 these regions display smaller enhancements (mean 12 ppb; max 52 ppb) consistent

with reduced precipitation and emissions. Similarly, while enhancements (mean 17 ppb; max 65 ppb) are seen during OND 2018, consistent with wetland emissions from South Sudan, even larger enhancements (mean 20 ppb; max 86 ppb) are present in OND 2019, particularly over South Sudan (figure 2). The mean XCH₄ enhancements in MAM 2018 and OND 2019 across East Africa are 33% and 18% larger than the equivalent season in the opposite year, consistent with the large positive seasonal precipitation anomalies (figure 1).

3.3. East African CH₄ emissions

The enhancements in the satellite data provide a useful indication of potential emission anomalies. However, to fully understand the behaviour of the fluxes a more formal Bayesian inversion is required. XCH₄ measurements from TROPOMI and GOSAT were assimilated into the LETKF inversion to provide monthly CH₄ emission estimates. The *a posteriori* CH₄ emission estimates corresponding to each set of data are generally consistent within their uncertainties (figure 3). Both sets of estimates show prominent emission peaks during MAM 2018 and particularly OND 2019. Our *a posteriori* emissions estimate from TROPOMI XCH₄ data in MAM 2018 is 6.2 ± 0.3 Tg CH₄ and in OND 2019 is 8.6 ± 0.3 Tg CH₄. These represent a 0.5 ± 0.2 Tg CH₄ (10%) and 2.3 ± 0.2 Tg CH₄ (37%) increase from MAM 2019

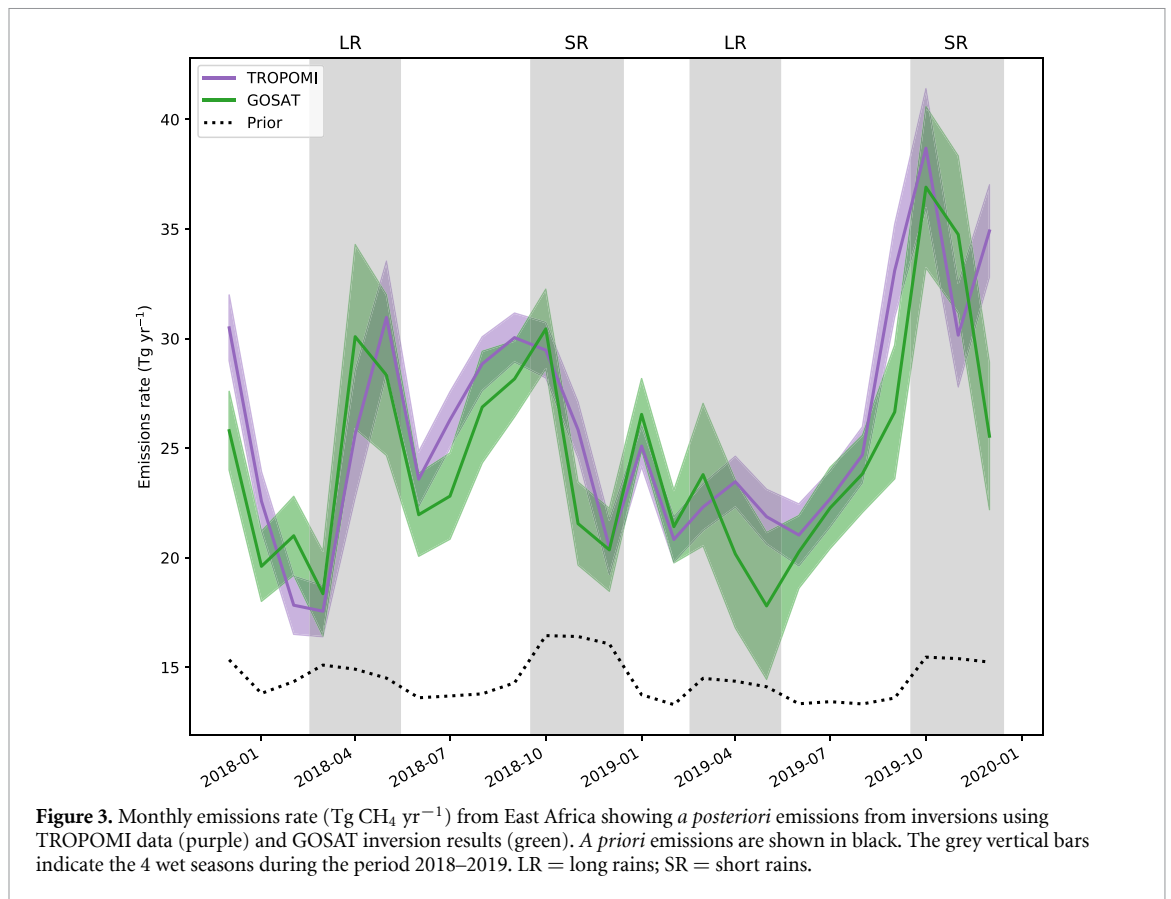


Figure 3. Monthly emissions rate ($\text{Tg CH}_4 \text{ yr}^{-1}$) from East Africa showing *a posteriori* emissions from inversions using TROPOMI data (purple) and GOSAT inversion results (green). *A priori* emissions are shown in black. The grey vertical bars indicate the 4 wet seasons during the period 2018–2019. LR = long rains; SR = short rains.

and OND 2018, respectively. We calculate similar *a posteriori* seasonal emissions inferred from GOSAT XCH₄ data of $6.4 \pm 0.5 \text{ Tg CH}_4$ and $8.1 \pm 0.5 \text{ Tg CH}_4$ in MAM 2018 and OND 2019, respectively, with an emissions difference in OND of $2.1 \pm 0.3 \text{ Tg CH}_4$ and a larger MAM difference of $1.2 \pm 0.3 \text{ Tg CH}_4$ (table S1).

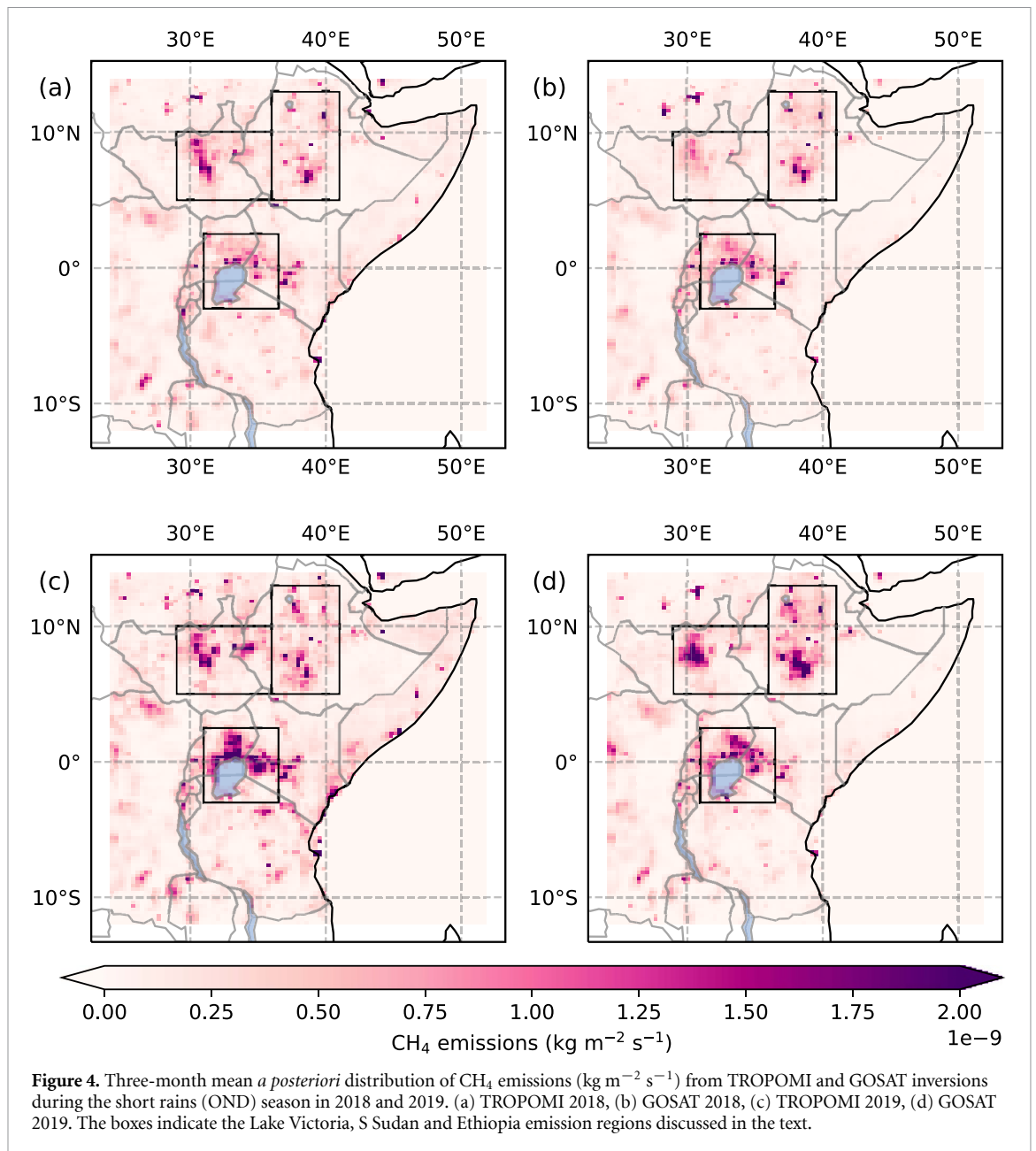
The additional seasonal pulses of CH₄ emissions in MAM 2018 and OND 2019 coincide with large growth rates of global atmospheric CH₄ of 8.5 ppb and 10.4 ppb in 2018 and 2019 respectively (Dlugokencky 2020). By incorporating these global mean CH₄ data into a one box-model calculation, global emissions growth is estimated to be 5 and 7 Tg CH₄ in the respective years, assuming a constant atmospheric lifetime (see appendix and figure S3). Therefore, the additional seasonal emissions pulses we report from East Africa, based on TROPOMI (GOSAT) data, represent 10 (24)% and 32 (30)% of the increase in global CH₄ emissions in 2018 and 2019 respectively. Although our calculation is subject to assumptions regarding the atmospheric loss rate of CH₄ it demonstrates that the seasonal East African emission pulses could account for a considerable fraction of the global emissions growth in 2018 and 2019.

The distribution of OND emissions in 2018 and 2019 from both TROPOMI and GOSAT derived estimates is shown in figure 4. Both estimates show increases in emissions in the region surrounding Lake Victoria. The TROPOMI estimates indicate an

increase of $0.7 \pm 0.1 \text{ Tg CH}_4$ from this region and the GOSAT inversions $0.4 \pm 0.3 \text{ Tg CH}_4$. The major regions of change from the GOSAT estimates are seen in S Sudan and Ethiopia with two distinct hotspots around 8° N . The increase in emissions from the S Sudan regions is $0.4 \pm 0.1 \text{ Tg CH}_4$, and from Ethiopia $0.8 \pm 0.2 \text{ Tg CH}_4$. The TROPOMI results indicate a smaller increase of $0.2 \pm 0.1 \text{ Tg CH}_4$ from both regions, but a change in the emissions distribution, with greater emissions in 2019 around the South Sudan/Ethiopia border in the Sobat basin. Greater emissions from this wetland region to the east of the Sudd, are consistent with significant positive soil moisture anomalies in OND 2019 (figure S4).

The simulated background component of the data is consistent between the two observational datasets. Therefore, differences in estimated emissions reflect differences in the spatial coverage and density of observations as well as any offsets in observed XCH₄ values. The sparser GOSAT coverage, relative to TROPOMI, can explain why emissions are generally confined to regions where *a priori* emissions are most prominent (figure S5).

We solve for total CH₄ emissions, and cannot directly determine the underlying source sectors behind the seasonal emissions pulses we find. However, we can make the crude assumption that the fractional contribution of each source sector in each grid cell is the same in the *a posteriori* distribution as in the *a priori*. Given this assumption, we find that the



largest component of the seasonal OND emissions peak in both years is from wetlands emissions (60%) followed by agriculture (15%), based on the difference between *a posteriori* emissions in OND and June. The division into sector emissions is limited because the *a priori* source sectors are not spatially distinct (figures S5–S6). However, at a qualitative level it suggests wetlands are the major driver of the *a posteriori* seasonal OND peak.

To further investigate the impact of the *a priori* distribution on the estimated short rains emission pulse of 2019 we conducted a sensitivity test, redistributing the wetland component of emissions to follow the soil moisture distribution (figure S7), since errors in the wetland inventory extent have been shown to cause a mismatch to satellite observations (Parker *et al* 2020b). Using our revised *a priori* emissions distribution we estimate *a posteriori* emissions

of $8.4 \pm 0.4 \text{ Tg CH}_4$ in OND 2019 that are close to the estimate ($8.6 \pm 0.3 \text{ Tg CH}_4$) corresponding to the main results, although with a different distribution of emissions (figure S7). We find the East Africa seasonal emission pulses are also relatively insensitive to changes in lateral boundary conditions and various assumptions made in the inversion method (figure S8).

Annual mean total CH₄ emission estimates from East Africa for 2018 and 2019 are 25 ± 1 and $27 \pm 1 \text{ Tg CH}_4 \text{ yr}^{-1}$ respectively. Our GOSAT derived estimates for both years are $24 \pm 1 \text{ Tg CH}_4 \text{ yr}^{-1}$. Results from both satellites are substantially larger than the *a priori* fluxes, the mean of which is $15 \text{ Tg CH}_4 \text{ yr}^{-1}$ in both years. Through scaling the relative *a priori* emissions of each source sector in each grid cell by the *a posteriori* ratio we find that, in June (when emissions are at a minimum) agricultural

emissions from livestock account for 60% of this difference between *a priori* and *a posteriori* emissions. A sensitivity test using *a priori* fluxes that are twice as large in all grid boxes returned the same annual mean emissions for East Africa, indicating the minimal impact of *a priori* emissions on our results at this regional scale (figure S9).

Our East African emissions estimates are slightly smaller than the estimate from previously published work for the 2011–2016 mean of 27 Tg CH₄ yr⁻¹ (Lunt *et al* 2019). We attribute this to differences in emissions from South Sudan. Our annual mean emission estimates for total CH₄ from S Sudan are 3.4 ± 0.2 Tg CH₄ yr⁻¹ in 2018–2019 from TROPOMI XCH₄ data and 3.4 ± 0.3 Tg CH₄ yr⁻¹ from GOSAT XCH₄ data, compared to the recently published estimates of 6.3 Tg CH₄ yr⁻¹ for 2015–2016 (Lunt *et al* 2019). Assuming a dependency on water table height, these estimates can be reconciled by GRACE LWE height anomalies which dropped from +2.6 cm in 2015–2016 to -1.5 cm in 2018, returning to levels closer to values in 2011–2012 when estimates from this previous study were 3.5 Tg CH₄ yr⁻¹ (Lunt *et al* 2019).

However, our estimates for the sum of all sources from S Sudan are inconsistent with another recent study which estimated emissions from only wetlands of 7.2 ± 3.2 Tg CH₄ yr⁻¹ in 2018–2019 using TROPOMI data and a mass balance method (Pandey *et al* 2020). A bias in the definition of the background concentration used by either approach will lead to larger or smaller XCH₄ enhancements and subsequent emission estimates. For instance, our sensitivity tests show that a 5 ppb positive bias in the background results in East African emissions that are larger by 6 Tg CH₄ yr⁻¹. However, we find that this bias translates into a S Sudan estimate that is larger by only 0.5 Tg CH₄ yr⁻¹, suggesting that the background contribution to the total XCH₄ column would have to be substantially smaller to reconcile the two estimates. When we relax our TROPOMI observation selection criteria to closely follow Pandey *et al* (2020), allowing greater aerosol loading and surface albedo thresholds, our *a posteriori* estimate for S Sudan increases to 4.6 Tg CH₄ yr⁻¹. While this partly helps to reconcile the emission difference the resulting emission distribution is forced to be unrealistic, and inconsistent with results using GOSAT data (supplementary material). A further explanation is likely to lie in the use of different meteorology fields (GEOS-FP vs ERA-5) and the use of a mass-balance method in Pandey *et al* (2020) versus the 3D modelling and EnKF approach used here.

4. Conclusions

We demonstrate how the extreme rainfall anomalies over East Africa in 2019 in particular, led to additional seasonal emissions of CH₄. The positive precipitation

anomalies in late 2019 continued into early 2020, resulting in the water levels of Lake Victoria reaching record-breaking levels (Wainwright *et al* 2020). A previous rapid increase in Lake Victoria water levels in the 1960s was estimated to lead to a doubling of the flooded extent of the Sudd wetlands in South Sudan (Sutcliffe and Parks 1999). Release rates from the dams controlling the outflow of Lake Victoria have been at unprecedentedly high levels in 2020 to mitigate the impacts of lakeside flooding. As a result, due to the greater water flows entering the White Nile we anticipate this should impact CH₄ emissions from downstream wetland regions such as the Sudd in the latter half of 2020. In the longer term, with climate models projecting that the frequency of the extreme positive values of the IOD increase under future climate (Cai *et al* 2018), it is important we take into account the disproportionately large contributions by East Africa to the global growth rate of atmospheric CH₄.

Data availability statement

GRACE/GRACE-FO Mascon data are available at <http://grace.jpl.nasa.gov>. TAMSAT data are available from www.tamsat.org.uk/data. The GOSAT v9.0 dataset is available at <https://doi.org/10.5285/18ef8247f52a4cb6a14013f8235cc1eb>. The presented material contains modified Copernicus TROPOMI CH₄ data, available from <ftp://ftp.sron.nl/open-access-data-2/TROPOMI/tropomi/ch4/>.

Acknowledgments

MFL and PIP gratefully acknowledge funding from the Methane Observations and Yearly Assessments (MOYA) project (NE/N015916/1) and the National Centre for Earth Observation funded by the National Environment Research Council (NE/R016518/1). The TROPOMI data processing was carried out on the Dutch national e-infrastructure with the support of the SURF Cooperative. RJP and HB are funded via the UK National Centre for Earth Observation (NE/R016518/1 and NE/N018079/1), and acknowledge funding from the ESA GHG-CCI and Copernicus C3S projects. We thank the Japanese Aerospace Exploration Agency, National Institute for Environmental Studies, and the Ministry of Environment for the GOSAT data and their continuous support as part of the Joint Research Agreement. The GOSAT data processing used the ALICE High Performance Computing Facility at the University of Leicester.

Appendix

To estimate the global growth of emissions we used a simple one-box model of the atmosphere. The change

in concentration over time through mass balance is given by:

$$\frac{dB}{dt} = Q - kB, \quad (\text{A1})$$

where B is the tropospheric concentration (Tg), Q is the emissions rate (Tg/yr) and k is the loss rate (yr^{-1}), proportional to one over the lifetime. Through integration of equation (A1) and rearrangement it can be shown (Jacob 1999) that the emissions at time, t are equal to:

$$Q_t = \frac{k(B_t - B_{t-1}e^{-k})}{(1 - e^{-k})} \quad (\text{A2})$$

We used annual mean CH_4 mole fraction data from the National Oceanic and Atmospheric Administration (NOAA) (Dlugokencky 2020). We used a conversion of tropospheric mole fraction to mass of $2.767 \text{ Tg CH}_4 \text{ ppb}^{-1}$ (Lassey et al 2007). We tuned the loss rate to match a steady state annual mean concentration of 1775 ppb with emissions in 2002–2006 of $546 \text{ Tg CH}_4 \text{ yr}^{-1}$ (Saunio et al 2017). Based on the NOAA annual mean data and these numbers we estimate global emissions of 586, 591 and $598 \text{ Tg CH}_4 \text{ yr}^{-1}$ in 2017, 2018 and 2019 respectively (figure S3). This represents a 5 and 7 Tg increase in global CH_4 emissions in 2018 and 2019 respectively. The box model calculation is highly simplified and assumes a constant loss rate of CH_4 from the atmosphere. A decreasing/increasing loss term over time would result in smaller/larger global emission estimates. Even so, at the global scale the mass balance approach provides a reasonable approximation to the evolution of atmospheric CH_4 , and show the East African emission pulses could account for a considerable fraction of the observed atmospheric growth.

ORCID iDs

Mark F Lunt  <https://orcid.org/0000-0002-0827-2137>

Paul I Palmer  <https://orcid.org/0000-0002-1487-0969>

Alba Lorente  <https://orcid.org/0000-0002-2287-4687>

Tobias Borsdorff  <https://orcid.org/0000-0002-4421-0187>

Jochen Landgraf  <https://orcid.org/0000-0002-6069-0598>

Robert J Parker  <https://orcid.org/0000-0002-0801-0831>

Hartmut Boesch  <https://orcid.org/0000-0003-3944-9879>

References

- Bey I et al 2001 Global modeling of tropospheric chemistry with assimilated meteorology: model description and evaluation *J. Geophys. Res.: Atmos.* **106** 23073–95
- Bloom A A, Bowman K W, Lee M, Turner A J, Schroeder R, Worden J R, Weidner R, McDonald K C and Jacob D J 2017 A global wetland methane emissions and uncertainty dataset for atmospheric chemical transport models (WetCHARTs version 1.0) *Geosci. Model Dev.* **10** 2141–56
- Bloom A A, Palmer P I, Fraser A and Reay D S 2012 Seasonal variability of tropical wetland CH_4 emissions: the role of the methanogen-available carbon pool *Biogeosciences* **9** 2821–30
- Bloom A A, Palmer P I, Fraser A, Reay D S and Frankenberg C 2010 Large-scale controls of methanogenesis inferred from methane and gravity spaceborne data *Science* **327** 322–5
- Butz A et al 2011 Toward accurate CO_2 and CH_4 observations from GOSAT *Geophys. Res. Lett.* **38** n/a–n/a
- Cai W, Wang G, Gan B, Wu L, Santoso A, Lin X, Chen Z, Jia F and Yamagata T 2018 Stabilised frequency of extreme positive Indian Ocean dipole under 1.5°C warming *Nat. Commun.* **9** 1419
- Charmley E et al 2016 A universal equation to predict methane production of forage-fed cattle in Australia *Anim. Prod. Sci.* **56** 169
- Christensen T R et al 2003 Factors controlling large scale variations in methane emissions from wetlands *Geophys. Res. Lett.* **30** 1414
- Dlugokencky E 2020 NOAA/ESRL (available at: www.esrl.noaa.gov/gmd/ccgg/trends_ch4/)
- Gedney N 2004 Climate feedback from wetland methane emissions *Geophys. Res. Lett.* **31** L20503
- Herrmann S M and Mohr K I 2011 A continental-scale classification of rainfall seasonality regimes in Africa based on gridded precipitation and land surface temperature products *J. Appl. Meteorol. Climatol.* **50** 2504–13
- Hu H, Hasekamp O, Butz A, Galli A, Landgraf J, de Brugh J A, Borsdorff T, Scheepmaker R and Aben I 2016 The operational methane retrieval algorithm for TROPOMI *Atmos. Meas. Tech.* **9** 5423–40
- Hu H, Landgraf J, Detmers R, Borsdorff T, de Brugh J A, Aben I, Butz A and Hasekamp O 2018 Toward global mapping of methane with TROPOMI: first results and intersatellite comparison to GOSAT *Geophys. Res. Lett.* **45** 3682–9
- Hunt B R, Kostelich E J and Szunyogh I 2007 Efficient data assimilation for spatiotemporal chaos: a local ensemble transform Kalman filter *Phys. D: Nonlinear Phenom.* **230** 112–26
- Jacob D J 1999 *Introduction to Atmospheric Chemistry* (Princeton, NJ: Princeton University Press)
- Kaiser J W et al 2012 Biomass burning emissions estimated with a global fire assimilation system based on observed fire radiative power *Biogeosciences* **9** 527–54
- Kilavi M, MacLeod D, Ambani M, Robbins J, Dankers R, Graham R, Helen T, Salih A and Todd M 2018 Extreme rainfall and flooding over central kenya including nairobi city during the long-rains season 2018: causes, predictability and potential for early warning and actions *Atmosphere* **9** 472
- Kuze A, Suto H, Nakajima M and Hamazaki T 2009 Thermal and near infrared sensor for carbon observation Fourier-transform spectrometer on the greenhouse gases observing satellite for greenhouse gases monitoring *Appl. Opt.* **48** 6716
- Landerer F W et al 2020 Extending the global mass change data record: GRACE follow-on instrument and science data performance *Geophys. Res. Lett.* **47** e2020GL088306
- Lassey K R, Etheridge D M, Lowe D C, Smith A M and Ferretti D F 2007 Centennial evolution of the atmospheric methane budget: what do the carbon isotopes tell us? *Atmos. Chem. Phys.* **7** 2119–39
- Liu J, Bowman K W and Lee M 2016 Comparison between the local ensemble transform Kalman filter (LETKF) and 4d-var in atmospheric CO_2 flux inversion with the Goddard earth observing system—chem model and the observation impact diagnostics from the LETKF *J. Geophys. Res.: Atmos.* **121** 13066–87

- Lorente A *et al* 2020 Methane retrieved from TROPOMI: improvement of the data product and validation of the first two years of measurements *Atmos. Meas. Tech. Discuss.* (<https://doi.org/10.5194/amt-2020-281>)
- Lu B and Ren H-L 2020 What caused the extreme Indian Ocean Dipole event in 2019? *Geophys. Res. Lett.* **47** e2020GL087768
- Lunt M F, Palmer P I, Feng L, Taylor C M, Boesch H and Parker R J 2019 An increase in methane emissions from tropical Africa between 2010 and 2016 inferred from satellite data *Atmos. Chem. Phys.* **19** 14721–40
- Maasakkers J D *et al* 2019 Global distribution of methane emissions, emission trends and OH concentrations and trends inferred from an inversion of GOSAT satellite data for 2010–2015 *Atmos. Chem. Phys.* **19** 7859–81
- Maidment R I *et al* 2017 A new, long-term daily satellite-based rainfall dataset for operational monitoring in Africa *Sci. Data* **4** 170063
- Maidment R I, Grimes D, Allan R P, Tarnavsky E, Stringer M, Hewison T, Roebeling R and Black E 2014 The 30 year TAMSAT african rainfall climatology and time series (TARCAT) data set *J. Geophys. Res.: Atmos.* **119** 10619–644
- McNorton J, Wilson C, Gloor M, Parker R J, Boesch H, Feng W, Hossaini R and Chipperfield M P 2018 Attribution of recent increases in atmospheric methane through 3-d inverse modelling *Atmos. Chem. Phys.* **18** 18149–68
- Miyazaki K, Eskes H J and Sudo K 2012 Global NO_x emission estimates derived from an assimilation of OMI tropospheric NO₂ columns *Atmos. Chem. Phys.* **12** 2263–88
- Moore T, Roulet N and Waddington J 1998 Uncertainty in predicting the effect of climatic change on the carbon cycling of Canadian peatlands *Clim. Change* **40** 229–45
- Ndung'u P W, Bebe B O, Ondiek J O, Butterbach-Bahl K, Merbold L and Goopy J P 2019 Improved region-specific emission factors for enteric methane emissions from cattle in smallholder mixed crop: livestock systems of Nandi County, Kenya *Animal Prod. Sci.* **59** 1136
- Pandey S *et al* 2017 Enhanced methane emissions from tropical wetlands during the 2011 La Niña *Sci. Rep.* **7** 45759
- Pandey S, Houweling S, Lorente A, Borsdorff T, Tsivlidou M, Bloom A A, Poulter B, Zhang Z and Aben I 2020 Using satellite data to identify the methane emission controls of south Sudan's wetlands *Biogeosci. Discuss.* (<https://doi.org/10.5194/bg-2020-251>)
- Parker R J *et al* 2011 Methane observations from the greenhouse gases observing SATellite: comparison to ground-based TCCON data and model calculations *Geophys. Res. Lett.* **38** L15807
- Parker R J *et al* 2020a A decade of GOSAT proxy satellite CH₄ observations *Earth Syst. Sci. Data* **12** 3383–412
- Parker R J, Wilson C, Bloom A A, Comyn-Platt E, Hayman G, McNorton J, Boesch H and Chipperfield M P 2020b Exploring constraints on a wetland methane emission ensemble (WetCHARTs) using GOSAT satellite observations *Biogeosciences* **17** 5669–91
- Rigby M *et al* 2017 Role of atmospheric oxidation in recent methane growth *Proc. Natl Acad. Sci.* **114** 5373–7
- Saji N H, Goswami B N, Vinayachandran P N and Yamagata T 1999 A dipole mode in the tropical Indian Ocean *Nature* **401** 360–3
- Sauniois M *et al* 2016 The global methane budget 2000–2012 *Earth Syst. Sci. Data* **8** 697–751
- Sauniois M *et al* 2017 Variability and quasi-decadal changes in the methane budget over the period 2000–2012 *Atmos. Chem. Phys.* **17** 11135–61
- Sauniois M *et al* 2020 The global methane budget 2000–2017 *Earth Syst. Sci. Data* **12** 1561–623
- Sutcliffe J V and Parks Y 1999 *The Hydrology of the Nile* (Wallingford: International Association of Hydrological Sciences)
- Tarnavsky E, Grimes D, Maidment R, Black E, Allan R P, Stringer M, Chadwick R and Kayitakire F 2014 Extension of the TAMSAT satellite-based rainfall monitoring over Africa and from 1983 to present *J. Appl. Meteorol. Climatol.* **53** 2805–22
- Turner A J *et al* 2015 Estimating global and north American methane emissions with high spatial resolution using GOSAT satellite data *Atmos. Chem. Phys.* **15** 7049–69
- Turner A J, Frankenberg C and Kort E A 2019 Interpreting contemporary trends in atmospheric methane *Proc. Natl Acad. Sci.* **116** 2805–13
- Wainwright C M, Finney D L, Kilavi M, Black E and Marsham J H 2020 Extreme rainfall in East Africa, October 2019–January 2020 and context under future climate change *Weather* **76** 26–31
- Wecht K J, Jacob D J, Frankenberg C, Jiang Z and Blake D R 2014 Mapping of north American methane emissions with high spatial resolution by inversion of SCIAMACHY satellite data *J. Geophys. Res.: Atmos.* **119** 7741–56
- Worden J R, Bloom A A, Pandey S, Jiang Z, Worden H M, Walker T W, Houweling S and Röckmann T 2017 Reduced biomass burning emissions reconcile conflicting estimates of the post-2006 atmospheric methane budget *Nat. Commun.* **8** 2227
- Wunch D, Toon G C, Blavier J-F L, Washenfelder R A, Notholt J, Connor B J, Griffith D W T, Sherlock V and Wennberg P O 2011 The total carbon column observing network *Phil. Trans. R. Soc. A* **369** 2087–112
- Zhang Z, Zimmermann N E, Calle L, Hurtt G, Chatterjee A and Poulter B 2018 Enhanced response of global wetland methane emissions to the 2015–2016 El Niño-southern oscillation event *Environ. Res. Lett.* **13** 074009